ONLINE FIRST July 10, 2026

Engineering Transactions, **74**, https://doi.org/10.24423/engtrans.2026.3596
Institute of Fundamental Technological Research Polish Academy of Sciences (IPPT PAN)
Université de Lorraine • Poznan University of Technology

Research Paper

Modeling Defect Detection in 3D-Printed Structures Using Ultrasonic Guided Waves

Ismaine ZITOUNI[1)*], Hassan RHIMINI[2)], Abdelkerim CHOUAF[2)]

[1)] *Interdisciplinary Laboratory of Fundamental and Applied Sciences, Ecole Normale Supérieure*
[2)] *Laboratory of Mechanics, Engineering and Innovation, National High School of Electricity and Mechanics*

Hassan II University of Casablanca
Casablanca, Morocco

[*]Corresponding Author: ismaine.zitouni.doc20@ensem.ac.ma

Carbon fiber-reinforced thermoplastic (CFRTP) composites are widely utilized in 3D printing via the fused filament fabrication (FFF) process. However, defects within printed components can compromise their performance. This study investigates the application of ultrasonic non-destructive testing (NDT) techniques to structures manufactured through FFF. Common printing defects, such as weak interlayer bonding, surface imperfections, and internal cracks, are simulated using a finite element (FE) model. The model analyzes how guided ultrasonic waves interact with these defects. The proposed methodology incorporates digital transducer control and evaluates the energy distribution among incident, reflected, and transmitted wave modes. Three representative defect types are modeled, and the approach is applied to two structural geometries: plates and pipes. The study investigates the correlation between defect size and the behavior of energy reflection and transmission. A signal processing approach is applied, using transducers positioned symmetrically along the wave propagation axis to detect mode conversion and analyze wave reflections and transmissions. The phenomenon of mode conversion is analyzed in detail, and the results are validated by ensuring energy-balance consistency.

Keywords: ultrasonic testing, finite element simulation, guided waves, defect detection, non-destructive testing.

Copyright © 2026 The Author(s).
Published by IPPT PAN. This work is licensed under the Creative Commons Attribution License CC BY 4.0 (https://creativecommons.org/licenses/by/4.0/).

1. Introduction

In recent years, 3D printing has undergone significant advancements across nearly all industrial branches, particularly in the automotive, aerospace, and healthcare industries. These industries have experienced rapid growth and diversification in printing technologies. The various techniques employed differ based

on the material used, the complexity of the part being printed, and considerations such as production and maintenance costs. For instance, methods such as selective laser melting (SLM) [1] and selective laser sintering (SLS) [2] are well-suited for metallic materials, while fused deposition modeling (FDM) [3] is commonly used for polymer filament printing. Despite these advances, numerous defects can still arise in printed components, stemming from a variety of causes. For example, defects may originate from materials themselves, such as low interfacial bonding between fibers and the matrix in composite structures [4, 5]. The fabrication process may also cause complications such as volumetric defects, porosities, cracks, and surface pitting [6]. Additionally, thermal effects during production can lead to problems, such as the formation of a thermally affected zone (TAZ) [7] notably in metal additive manufacturing processes involving welding. Given these potential defects, it is crucial to monitor and assess the integrity of such structures. Ultrasonic guided waves (UGWs) [8, 9] present a promising method for non-destructive testing (NDT) of these types of structures. They are highly effective for propagating over long distances with minimal attenuation, making them ideal for assessing structural integrity of components. To perform accurate NDT using UGWs, it is essential to understand the wave dispersion characteristics. The transducer must generate frequencies corresponding to specific modes indicated by the dispersion curves. Ultrasonic sensors are then used to measure the normal displacements on the surface of the structure being tested. Post-processing techniques, such as signal analysis using the Fourier transform, wavelets, or other methods, are essential for detecting and characterizing potential defects within a structure. Several researchers developed numerical models to simulate the propagation of UGWs in various structures. For example, De Luca *et al.* [10] utilized a finite element (FE) model in ABAQUS to study UGW propagation in a carbon fiber reinforced polymer (CFRP) laminated plate, analyzing how defect size and orientation impact structural integrity. Chui *et al.* [11] focused on delamination detection in a 3D laminate composed of four composite layers. Rhimini *et al.* [9] explored the interaction of UGWs with an embedded volumetric defect in a three-layer aluminum/epoxy/aluminum assembly, also using ABAQUS. In that study, post-processing involved applying a double Fourier transform to the data. In recent years, several researchers have started investigating defect detection in 3D-printed parts using ultrasound. Among them, Everton *et al.* [12] focused on identifying sub-surface defects through laser-generated ultrasound. Cummings *et al.* [13] developed an in situ method for detecting defects as they arise in plastic parts produced by the FDM process, although post-processing of the data still presents significant challenges. Caminero *et al.* [14] employed ultrasound combined with the phased array technique to assess damage in laminated 3D-printed composites. Despite these efforts, the use of UGWs for defect

detection remains underexplored, and post-processing techniques for interpreting the results continue to be a major hurdle.

In this study, we aim to carry out a numerical non-destructive inspection of CFRTP composite parts using guided waves [15]. CFRTP composites are widely used in filament-based manufacturing processes due to their superior mechanical properties compared with those of pure thermoplastics [16, 17]. Additionally, the high prototyping flexibility and various printing parameters specific to the FDM process, such as raster angle and filament size, enable the fabrication of complex structures with CFRTP, making it a popular choice in industries such as automotive manufacturing and aerospace. Nevertheless, the stiffness of printed CFRTP composites can deteriorate due to imperfections such as ruptures, layer detachment, and notches, often caused by inappropriate printing parameters [18, 19].

In our analysis, the structures considered exhibit rectangular notches and cracks. To inspect these structures, we first generated dispersion curves for the material, representing the frequency-wavenumber pairs that could excite UGWs in our waveguide [20, 21]. Additionally, we plotted normalized displacement profiles with energy flow across the section by applying a spatial distribution of displacements over 10 cycles, using a Hanning window centered at the excitation frequency for weighting these displacements.

Based on these elements, we developed a numerical FE simulation of the UGW implementation process in composite plates and cylindrical pipes. We also simulated the acquisition of signals both before and after encountering a defect using FE software. By calculating reflection and transmission coefficients, we analyzed how defect size and position affect the selection of the appropriate ultrasonic mode for inspection. As the defect size increases, the reflected wave packet also increases. Moreover, when the defect is asymmetrically positioned with respect to the median plane of the plates, mode conversion occurs, a phenomenon we addressed using a technique based on summing and subtracting the signals captured by the ultrasonic transducers.

2. Theory of UGWs

2.1. Dispersion network

We analyze the propagation of UGWs through a composite waveguide. The material under consideration is a CFRTP commonly used in 3D printing, particularly in the FDM process. UGWs enable comprehensive scanning of the entire waveguide structure. However, to achieve this, it is essential to understand the dispersion patterns of these waves. Since UGWs are highly frequency-dependent, even a small frequency change can significantly alter their behavior. These dis-

persion patterns, known as dispersion curves, identify the frequency (f) and wave number (k) pairs that can generate UGWs within the composite waveguide. Various methods have been applied to characterize this dispersive behavior. These approaches include analytical techniques to find the zeros of a function [22], as well as numerical techniques to plot these curves [23]. In our study, we implemented a MATLAB program that uses a numerical spectral method [22] to plot dispersion curves for composite materials. The method applies a spectral scheme to approximate the differential equations governing motion and the associated boundary conditions. By determining the eigenvalues (frequencies) for a specified range of wavenumbers and using a vibrational state-based mode separation algorithm, we obtain dispersion curves in terms of frequency and wavenumber. Additionally, we can represent these curves in other forms, such as phase velocity V_p versus frequency or group velocity V_g versus frequency, which provide insights into the energy transport characteristics of the wave packet.

We consider two waveguides. The first is a 4 mm thick CFRTP composite plate (Fig. 1a) and the second is a CFRTP composite pipeline with an inner radius of 50 mm and an outer radius of 56 mm (Fig. 1b). The values of the components of the elastic stiffness tensor and the density of the composite are shown in Table 1. We note that the stiffness constants are expressed in the Cartesian system.

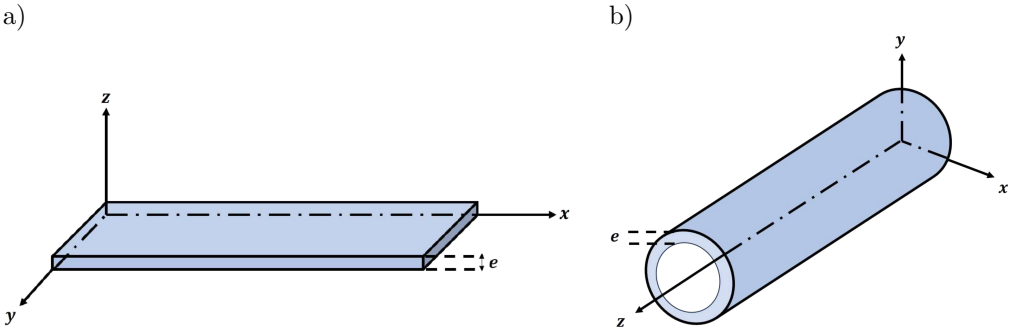

FIG. 1. a) Planar waveguide, b) cylindrical waveguide; (x, y, z)-Cartesian coordinate system, e-waveguide thickness.

TABLE 1. Material properties of the CFRTP composite [4].

Density [g/cm^3]	$C'_{11} = C'_{22} = C'_{33}$	$C'_{12} = C'_{13}$	$C'_{55} = C'_{66}$	C'_{44}	C'_{23}
1.6	43.3294	6.4745	9.51	18.4291	6.4712

Figure 2a presents the dispersion curves for the CFRTP composite plate in in the frequency-thickness product versus phase velocity plane. The plate exhibits Lamb-wave modes, including symmetric modes (S_n) and antisymmetric modes (A_n) with respect to the propagation planes. The fundamental modes, denoted as S_0 and A_0, are commonly used in UGW non-destructive testing [24, 25].

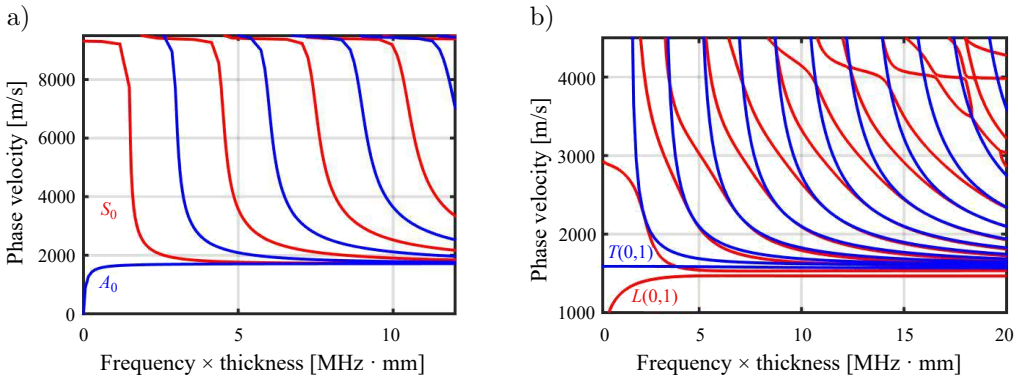

FIG. 2. Dispersion curves generated using the spectral method for a CFRTP composite plate with a 4 mm thickness (a) and a cylindrical pipe with an inner radius of 50 mm and an outer radius of 56 mm (b).

Figure 3 illustrates the vibrational states (von Mises stress) of the plate under these modes. We can see that the symmetrical S_n mode is symmetric with respect to the u_x displacement (displacement in the direction of propagation x) and antisymmetric with respect to the u_y displacement (displacement normal to the direction of propagation). The opposite behavior is observed for the antisymmetric mode A_n.

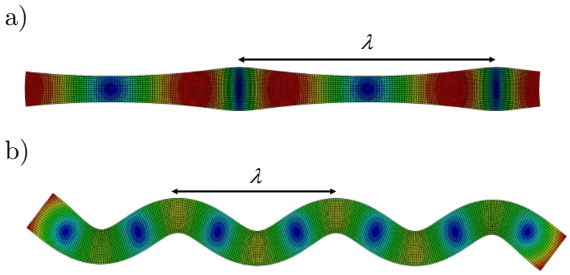

FIG. 3. Vibrational states of the plate: a) symmetrical Lamb mode S_n, b) antisymmetrical Lamb mode A_n. λ represent the wavelength.

Figure 2b shows the dispersion curves of the CFRTP composite cylindrical pipe. Due to the pipe curvature, the symmetry in vibration is lost [26], resulting in longitudinal modes $L(0,n)$ and torsional modes $T(0,n)$. Additional modes, such as flexural modes $F(m,n)$, are also present; however, these are excluded from our study. The vibration states of the pipe under the various modes are displayed in Fig. 4.

Here, n represents the mode index, determined by the order in which the mode appears at low frequencies, and m represents the order of the flexural mode.

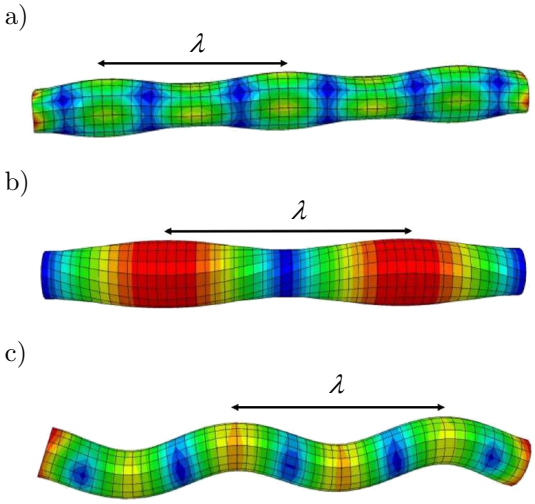

Fig. 4. Vibrational states of the cylindrical pipe: a) longitudinal mode $L(0,n)$, b) torsional mode $T(0,n)$, c) flexural mode $F(m,n)$.

2.2. Field of displacement

Nayfeh *et al.* [27] proposed the expression for displacement fields that describe the propagation of a harmonic wave in plane and cylindrical structures that are homogenous and anisotropic in shape:

$$\begin{cases} (u_x, u_y, u_z) = \sum_{q=1}^{6} (1, V_q, W_q) U_{1q} e^{ik(x+\alpha_q z - ct)}, \\ (u_r, u_\theta, u_z) = U_\beta^{mn}(r) \Theta_\beta^{mn}(m\theta) e^{i(\omega t - k^{mn} z)}, \end{cases} \tag{2.1}$$

where q is the summation index, x is the UGW propagation direction, c is the wave phase velocity, k is the wavenumber, U_{1q}, V_q, W_q are the displacement amplitudes [27], and α_q is the ratio between the wavenumbers in the x- and z-directions. Furthermore, U_β^{mn} and the sinusoidal function Θ_β^{mn} are the radial and circumferential components of velocity, respectively.

3. Numerical simulation

3.1. Formulation

We employ the finite element method (FEM), where the structure is discretized into FEs. Within each element, the displacement field is approximated using interpolation functions at each node, resulting in the so-called nodal displacements. The global equation system is then constructed by assembling these

individual element displacements. For the undamped case, the system is expressed as follows:

$$[\mathrm{M}]\{\ddot{\mathrm{U}}\} + [\mathrm{K}]\{\mathrm{U}\} = \{\mathrm{F}\}, \tag{3.1}$$

where [M] represent the global mass matrix, [K] is the global stiffness matrix, {U} is the global displacement vector, $\{\ddot{\mathrm{U}}\}$ is the global acceleration vector, and {F} is the global force vector.

In order to solve Eq. (3.1), we apply Newmark's method [28], which approximates the spatial partial derivatives. By utilizing extended mean value theorem, Newmark's method provides the following approximation to solve the first time derivative:

$$\{\dot{\mathrm{U}}_{t+\Delta t}\} = \{\dot{\mathrm{U}}_t\} + \Delta t\{\ddot{\mathrm{U}}_\gamma\} \tag{3.2}$$

with

$$\{\ddot{\mathrm{U}}_\gamma\} = (1-\gamma)\{\ddot{\mathrm{U}}_t\} + \gamma\{\ddot{\mathrm{U}}_{t+\Delta t}\}. \tag{3.3}$$

Since we have partial derivatives with respect to time in the acceleration vector, the theorem can also be written as

$$\{\mathrm{U}_{t+\Delta t}\} = \{\mathrm{U}_t\} + \Delta t\{\dot{\mathrm{U}}_t\} + \Delta t^2((1-\beta)\{\ddot{\mathrm{U}}_t\} + \beta\{\ddot{\mathrm{U}}_{t+\Delta t}\}), \tag{3.4}$$

where γ and β are the Newmark integration parameters, and Δt is the time step.

3.2. FE analysis model

We examine the propagation of UGWs in two types of CFRTP structures. The first structure is a homogeneous plate with a length of $L = 500\,\mathrm{mm}$ and a thickness of $e = 4\,\mathrm{mm}$. The second structure is a hollow cylindrical pipe with an inner radius of 50 mm, an outer radius of 56 mm, and a length of $L = 600\,\mathrm{mm}$. We consider a linear homogeneous dynamic calculation with no damping. The waveguide is initially not subjected to any stress, and the contact between the sensors and the structure is considered to be perfect. The small-perturbation assumption is also applied.

This study addresses a spatial-temporal problem and is simulated in ABAQUS. Details regarding simulation the parameters, including the spatial and temporal discretization steps Δx and Δy, will be provided later. To mesh our models, we select a control frequency of $f = 500\,\mathrm{kHz}$ (based on the dispersion curves) and use an element size of 0.5 mm, which meets the following condition [29]:

$$\max(\Delta x, \Delta y) \leq \frac{\lambda_{\min}}{10}, \tag{3.5}$$

where $\lambda_{\min}$ is the minimum wavelength [29].

This criterion specifies that, to ensure computational convergence, the element size used to discretize the waveguide should be no larger than one-tenth of the smallest wavelength of the propagating modes in the structure.

For time discretization, ensuring convergence in ultrasonic simulations demands that the shortest wavelength within the UGW pulse needs to be divided into at least 20 nodes. For a frequency of $f = 500\,\text{kHz}$, we get a temporal step of $0.1\,\mu\text{s}$, satisfying the following condition [30]:

$$\Delta t = \frac{1}{20f}, \tag{3.6}$$

where f is the mode frequency selected to produce ultrasonic guided-wave mode.

3.3. UGW generation

To numerically generate UGWs in waveguides, several researchers have modeled the excitation signal as a specific point force, typically represented by a sinusoidal waveform modified by a Hanning window [31, 32]. Other studies have employed piezoelectric transducers to generate UGWs by applying nodal loads around the circumference of a circle [32]. Additionally, another approach incorporated the Snell–Descartes laws to determine the wave incidence angle [32]. Despite the advantages of these methods, using a cyclic force can lead to edge reflection issues. This problem has been addressed in two ways: either by treating the boundary conditions as absorbing (resulting in no reflection) or by applying post-processing techniques to the acquired signals. To mitigate these issues and ensure the excitation of the desired mode, Rhimini *et al.* [9] utilized analytical displacements through the thickness of an isotropic multilayer laminate to effectively excite the Lamb-wave modes.

In this study, we focus on the latter approach to model the propagation of UGWs in both an anisotropic plate and a cylindrical pipe. Excitation based on analytical displacements scaled by acoustic power is applied. For the plate, we will generate the antisymetrical A_0 mode according to previous research that has shown that the S_0 and A_0 modes are the most commonly utilized in ultrasonic inspection, as they are situated at low and high frequencies, respectively. Additionally, the mode conversion phenomena associated with these modes are relatively straightforward [24, 25] and both can be generated at low frequency values. For the cylindrical pipe, the first longitudinal mode $L(0,1)$ is selected [33, 34].

Equation (2.1) provides the analytical displacement field that contains two components: the first component describes the spatial coordinate and the second one the temporal coordinate. The spatial component describes the mode shape generated across the thickness of the waveguide. For example, the chosen A_0

mode shows an antisymmetric longitudinal displacement (blue curve in Fig. 5a) and a symmetric transverse displacement throughout the plate thickness (red curve in Fig. 5a). Figure 5b displays the displacement profiles for the chosen longitudinal mode $L(0,1)$.

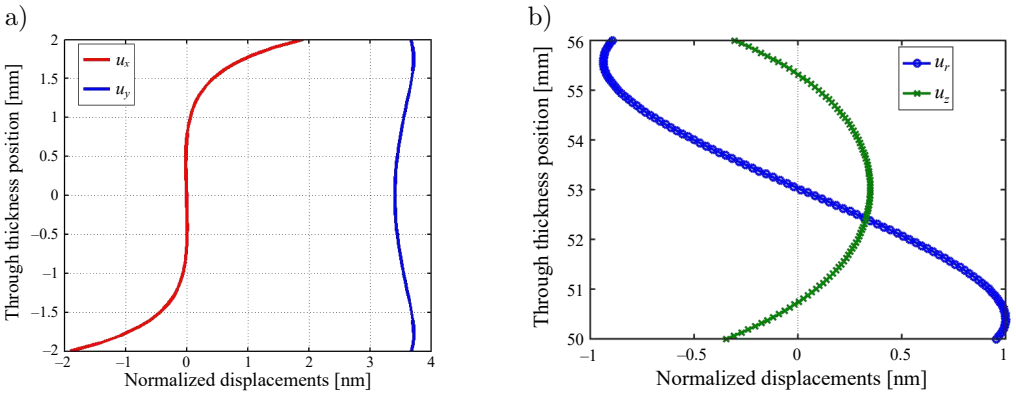

FIG. 5. Normalized analytical displacements scaled by acoustic power of the selected mode A_0 of the composite plate ($f = 500\,\mathrm{kHz}$, $k = 1431\,\mathrm{m}^{-1}$) (a) and the $L(0,1)$ mode of the composite pipe corresponding to the pair ($f = 500\,\mathrm{kHz}$, $k = 67\,\mathrm{m}^{-1}$) (b).

The temporal component is represented by the exponential term, resulting in the analytical spatial displacements oscillating according to either a cosine or sine function. The displacement fields can be expressed directly as functions of cosine or sine in isotropic materials [27]. However, in the case of highly anisotropic materials, such as the CFRTP in our study, it is not possible to definitively determine if the displacements are described by a cosine or sine dependance. To address this, during mapping spatial displacements at a particular position x and constant time t, the exponential term is solely dependent on the z-coordinate ($e^{i\varphi} = \cos(\varphi) + i\sin(\varphi)$). Thus, an imaginary displacement corresponds to a sine function, whereas a real displacement corresponds to a cosine function. For the plate, the displacement u_x follows a sine function, while the displacement u_z follows a cosine function (mode A_0). The same approach is applied to the $L(0,1)$ mode.

The spatial displacement distribution is used for 10 cycles, with weighting based on a Hanning window centered around the excitation frequency [35]. The use of a Hanning window excludes disturbances from the incoming signal (Fig. 6).

3.4. Inspection of the plate

On the left side of the plate, UGWs are induced to travel through its thickness. Transducers are placed on the plate surfaces $y = \pm h$ to track their move-

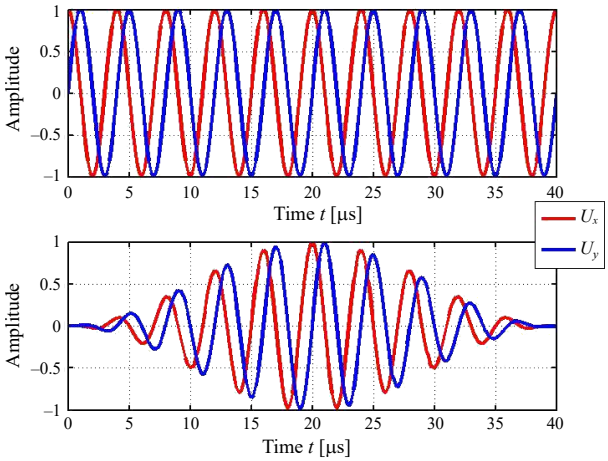

FIG. 6. Hanning window applied to the incident signal of the CFRTP composite plate.

ment along the plate, before and after the defect. Proper positioning of these transducers with respect to the plate edges and the defect is critical. UGWs consist of propagating modes, which are utilized in inspection, and evanescent modes [36, 37]. Due to their pronounced attenuation in the material, evanescent modes are not viable for ultrasonic non-destructive testing of large-scale structures. Evanescent modes become evident when reflections occur due to the plate edges or defects. Consequently, ultrasonic sensors placed close to the defect or the edge of the structure may pick up signals not only from the propagating modes but also from the evanescent modes. This can complicate the interpretation of the results, particularly if there is insufficient information regarding the characteristics of the evanescent waves. In this study, the transducers are positioned to maintain a minimum distance of at least 10 mm from both the defect and the plate edge. The selected transducers measure the displacements u_x and u_y at 180 nodes along the plate interface, with the nodes spaced evenly at 0.5 mm (mesh step). In scenarios where the defect location is unknown (as in real cases), it is essential to conduct a thorough investigation of the evanescent modes to understand and effectively address near-field wave-defect interaction phenomena.

Temporal displacements at the plate upper and lower surfaces, before the defect, are acquired using transducers 1 and 2. After the defect, transducers 3 and 4 record the temporal displacements at the upper and lower surfaces of the plate (Fig. 7). Transducers 1 and 2 record signals that encompass two wave packets. The first one originates from incident wave and the second one is due to wave reflection. The signals collected by transducers 3 and 4 corresponds to the transmission of the wave across the defect. The arrangement places transducer 1 opposite transducer 3, and transducer 2 opposite transducer 4. This configura-

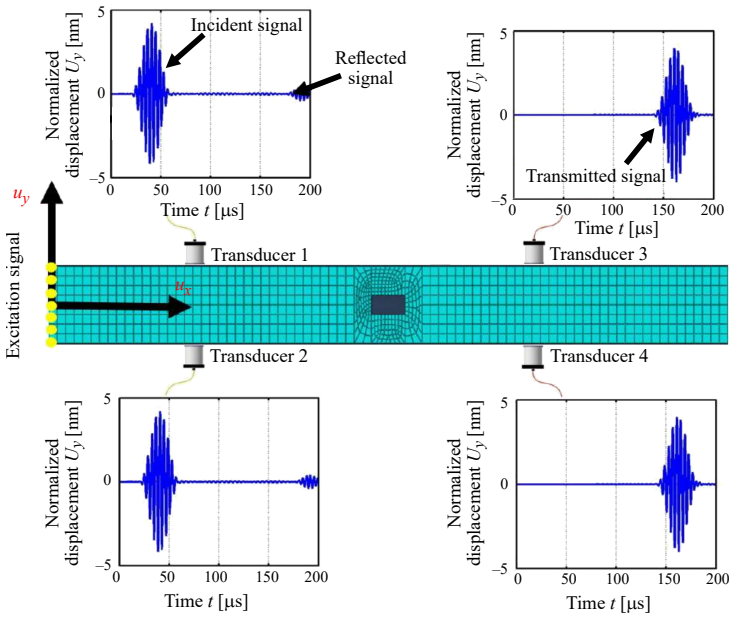

FIG. 7. Inspection of a symmetric defect in the composite CFRTP plate using the selected A_0 mode ($k = 1431\,\mathrm{m}^{-1}$, $f = 500\,\mathrm{kHz}$); $p = 2\,\mathrm{mm}$ and $w = 1\,\mathrm{mm}$.

tion allows us to determine the defect position, by assessing the time of flight between the incident and reflected waves, since we know in advance the phase velocity of the emitted wave. Additionally, the nature of the modes in the reflected and transmitted wave packets can be identified by examining the symmetry and antisymmetry characteristics of the S_0 and A_0 modes. To distinguish the modes present in the reflected and transmitted waves, some researchers utilized tools such as the 2D FFT of the recorded signals and the wavelet transform [9, 28].

In the initial step, the notch is assumed to be symmetrically located with respect to the plate median plane. The presented configuration prevents mode conversion. We first excite the A_0 mode, and the wave reaches the defect. The energy of this mode is partly reflected and partly transmitted, while the A_0 mode nature is preserved throughout the interaction. Subsequently, an asymmetric positioning of the notch relative to the plate median plane is considered. In this scenario, as the mode interacts with the defect, the reflected and transmitted wave packets include energy contributions from both the incident mode and the converted mode due to mode conversion phenomena. We therefore focus on assessing the influence of the notch dimensions and position on mode conversion and energy distribution.

Initially, we vary the defect parameters (length p and height w) and compute the energy coefficients of the reflection and transmission. The accuracy of the

calculations presented is monitored through the energy balance. Equation (3.7) and Eq. (3.8) report the formulas of the energy coefficients:

$$R = \frac{\phi_r}{\phi_i}, \tag{3.7}$$

$$T = \frac{\phi_t}{\phi_i}, \tag{3.8}$$

where ϕ_r, ϕ_t, and ϕ_i are the reflected, transmitted, and incident energy flows, respectively.

The reflection and transmission coefficients and the associated error are presented in Table 2. Only the A_0 and S_0 modes coexist in the plate because a frequency below the A_1 mode cut-off frequency is chosen. The tested specimens exhibit differences in defect length and height. As the defect length increases ($p\uparrow$), indicating a tendency toward a longitudinal crack, the reflected energy rises while the transmitted energy decreases, maintaining an overall energy balance close to unity. Similarly, increasing the defect height ($w\uparrow$, transverse crack) results in a higher reflection coefficient and a lower transmission coefficient.

TABLE 2. Energy coefficients describing the interaction of the first two fundamental modes A_0 and S_0 of the composite plate with defects of various dimensions.

Selected modes	Defect parameters (p = length, w = height) [mm]	Reflection coefficient (R)	Transmission coefficient (T)	Energy conservation ($R+T$)	Error [%]
Fundamental antisymmetric mode A_0 of the plate ($k = 1431\,\mathrm{m}^{-1}$, $f = 500\,\mathrm{kHz}$)	$p = 2$, $w = 1$	0.095	0.9093	1.0043	0.43
	$p = 5$, $w = 1$	0.7845	0.2364	1.0209	2.09
	$p = 1$, $w = 1$	0.0076	0.9927	1.0003	0.03
	$p = 1$, $w = 3$	0.8956	0.1134	1.0090	0.90
Fundamental symmetric mode S_0 of the plate ($k = 621\,\mathrm{m}^{-1}$, $f = 500\,\mathrm{kHz}$)	$p = 2$, $w = 1$	0.086	0.907	0.993	0.7
	$p = 5$, $w = 1$	0.8502	0.1672	1.0174	1.74
	$p = 1$, $w = 1$	0.0023	0.9966	0.9989	0.11
	$p = 1$, $w = 3$	0.8534	0.1542	1.0076	0.76

Figure 8 shows the scan of a plate that contains a defect asymmetrically positioned with respect to the median axis x. Two reflected signals are observed by transducers 1 and 2, while transducers 3 and 4 display two transmitted signals. This is due to the phenomenon of mode conversion. The A_0 mode generated initially interacts with the defect, reflecting a portion of its energy that depends on the defect dimensions. In this case, the reflected energy is split into two wave packets, a pattern also observed in the transmitted signals. To identify the type

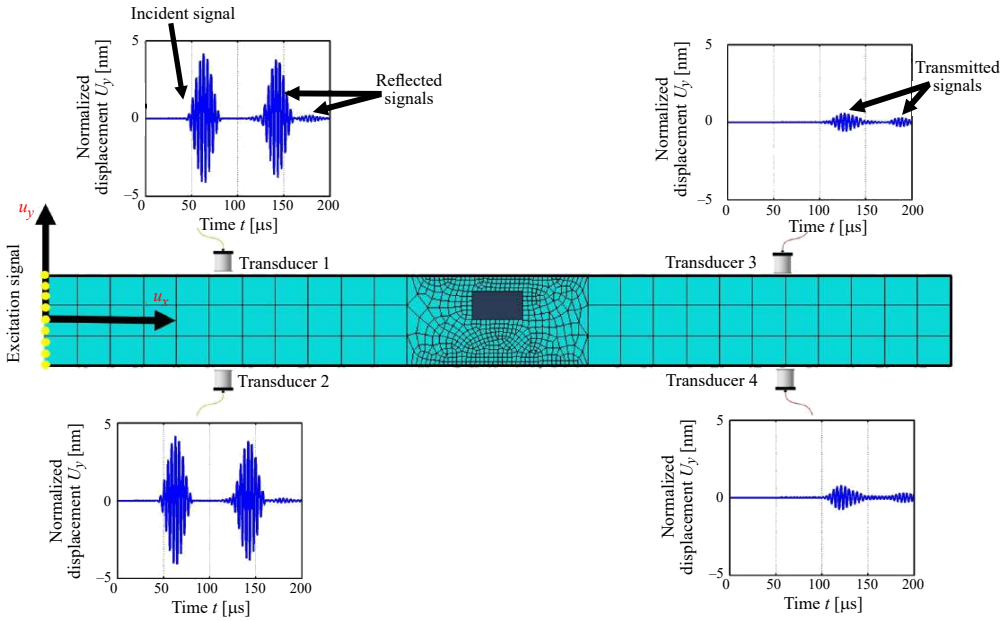

FIG. 8. Inspection of an asymmetrical defect in the composite CFRTP plate using the selected A_0 mode ($k = 1431\,\mathrm{m}^{-1}$, $f = 500\,\mathrm{kHz}$); $p = 2\,\mathrm{mm}$, $w = 1.5\,\mathrm{mm}$.

of reflected mode, several authors have applied the Fourier transform or wavelet transform [9, 27] to the recorded signal, enabling a transformation from the (X, t) domain to the (k, f) domain. This (k, f) domain represents the numerically obtained dispersion curves. By comparing these curves with analytically derived curves, the reflected and transmitted modes can be identified. In this study, we propose a new method based on the symmetry of propagating modes to characterize the mode conversion phenomenon. Specifically, a symmetric mode is defined by symmetric longitudinal displacement $(u_x(+d) \times u_x(-d) > 0)$ and antisymmetric transverse displacement $(u_y(+d) \times u_y(-d) < 0)$, while an antisymmetric mode exhibits the opposite behavior $(u_x(+d) \times u_x(-d) < 0$, $u_y(+d) \times u_y(-d) > 0)$ (see Fig. 3). By summing the signals from transducers 1 and 2 and separately from 3 and 4, the antisymmetric modes are suppressed, leaving only the symmetric modes. The symmetric modes can be filtered out by subtracting the signals from transducers 1 and 2 and 3 and 4, leaving only the antisymmetric modes. Through this approach, the reflected captured signal contains a component that corresponds to the A_0 mode. The other component is due to the conversion between A_0 and S_0 modes. A similar observation applies to the transmitted wave packet.

We then calculate the energy coefficients for reflection and transmission and report the results in Table 3. Two signals are observed in the reflected wave packet due to the defect asymmetric location relative to the propagation axis. By

TABLE 3. Energy coefficients describing the interaction of the A_0 and S_0 modes with an asymmetrically positioned defect.

Mode	Reflection coefficient (R)	Transmission coefficient (T)	Energy conservation ($R+T$)	Error [%]
Fundamental antisymmetric mode A_0 of the plate	0.310 A_0 0.227 S_0	0.309 A_0 0.183 S_0	1.029	2.9

applying the summation and subtraction technique, we determine the proportion of the reflected energy that retained the original mode (A_0, $R = 0.8334$) and the proportion that underwent mode conversion (A_0–S_0, $R = 0.023$). The defect dimensions play a role in determining these values. Similar conversion results were obtained for the transmitted wave packet.

Next, we analyzed the case of an inclined defect with an inclination angle of 45° relative to the propagation axis. Figure 9 shows the scan of the composite plate with an inclined defect. In the reflection region (transducers 1 and 2), two reflected wave packets were observed, and a similar pattern also appears in the transmission region (transducers 3 and 4). This indicates that an inclined defect induces mode conversion. To quantify the reflected and transmitted energy, we applied the summation and subtraction method (as described previously) and calculated the energy coefficients, which is presented in Table 4.

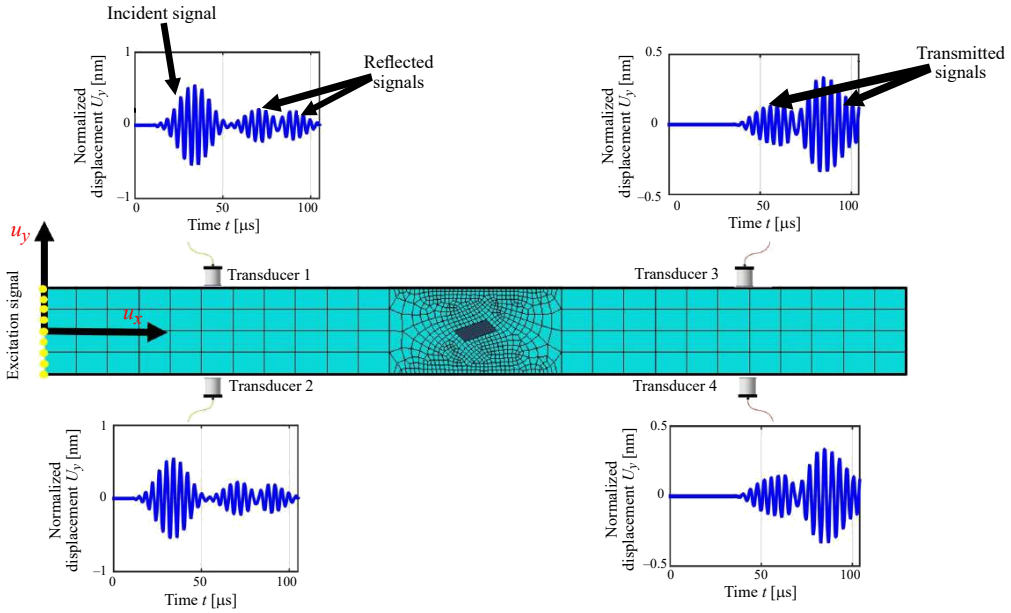

FIG. 9. Inspection of an inclined defect in the composite CFRTP plate using the selected A_0 mode ($k = 1431\,\mathrm{m}^{-1}$, $f = 500\,\mathrm{kHz}$); $p = 2\,\mathrm{mm}$, $w = 1\,\mathrm{mm}$.

TABLE 4. Energy coefficients describing the interaction of the A_0 and S_0 modes with the inclined defect.

Mode	Reflection coefficient (R)	Transmission coefficient (T)	Energy conservation ($R+T$)	Error [%]
Fundamental antisymmetric mode A_0 of the plate	0.8334 A_0 0.023 S_0	0.08 A_0 0.048 S_0	0.9764	2.32

The results indicate a clear presence of A_0–S_0 mode conversion in both the reflected and transmitted wave packets. Additionally, the inclined defect resulted in an almost equal distribution of reflected and transmitted energy.

3.5. Inspection of the pipe

We now consider a cylindrical pipe with a rectangular notch defect. We generate a longitudinal $L(0,1)$ mode along the pipe radius. Two transducers are used: one to capture the reflected energy and the other to capture the transmitted energy. We observe two reflected and two transmitted wave packets (Fig. 10), suggesting the occurrence of mode conversion [32].

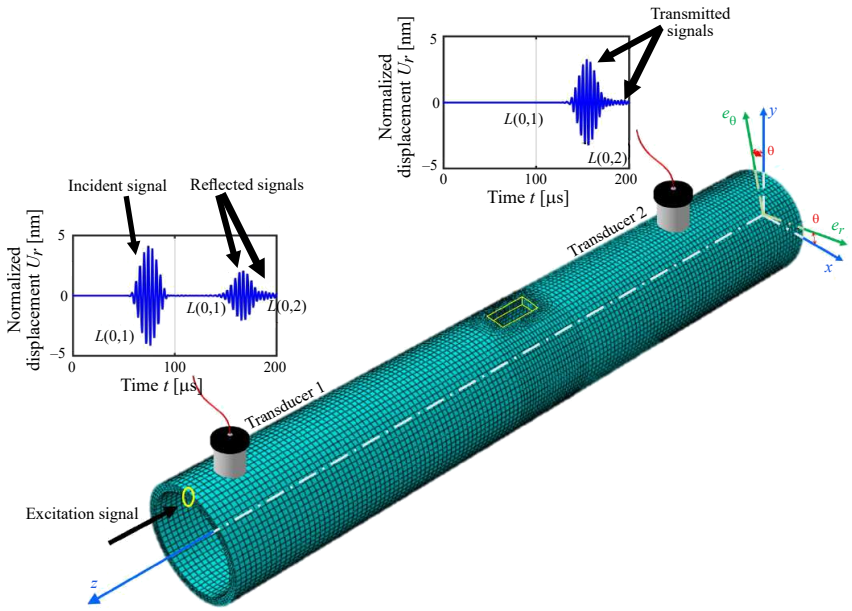

FIG. 10. Scan of the CFRTP composite cylindrical pipe using the longitudinal $L(0,1)$ mode, ($f = 500\,\mathrm{kHz}$, $k = 67\,\mathrm{m}^{-1}$) with a defect dimension ratio of $p/w = 3$.

The cylindrical geometry of the pipe disrupts mode symmetry (as shown by the dispersion curves, Fig. 2b), which prevents the use of the previously

proposed summation and subtraction method. To address this, we analyze the phase velocity to identify the modes present in the reflected and transmitted wave packets. Given the analytical phase velocity for the generated mode with $f = 500\,\text{kHz}$ and $k = 65\,\text{m}^{-1}$ is $V_p = 4688\,\text{m/s}$, we calculate the travel time between the incident and reflected waves [38]. Using the known distance between the transducer and the defect, we find a numerical phase velocity of $V_p = 4679\,\text{m/s}$, corresponding to the $L(0,1)$ mode (in close agreement with the analytical prediction). A second phase velocity is $V_p = 9809\,\text{m/s}$, aligning with the $L(0,2)$ mode (analytical value $V_p = 9817\,\text{m/s}$). We then compute the energy coefficients for different length-to-height (p/w) and height-to-length (w/p) ratios of the defect, and the results are presented in Fig. 11. Figure 11a shows that as the p/w ratio increases (indicating a more circumferential crack), the reflected energy rises while the transmitted energy decreases, maintaining an energy balance close to unity. Conversely, in Fig. 11b, an increase in the w/p ratio (indicating a more longitudinal crack) results in a decrease in reflected energy and an increase in transmitted energy. Thus, when the defect type is unknown, the defect dimensional ratio and therefore its nature can be inferred from the energy coefficient trends shown in Fig. 11. Experimentally, in order to inspect plates and pipelines using UGWs, several authors have used PZT transducers [39, 40] (known for their low weight and ease of bonding to the waveguide surface without signal loss) to detect signals before and after the defect.

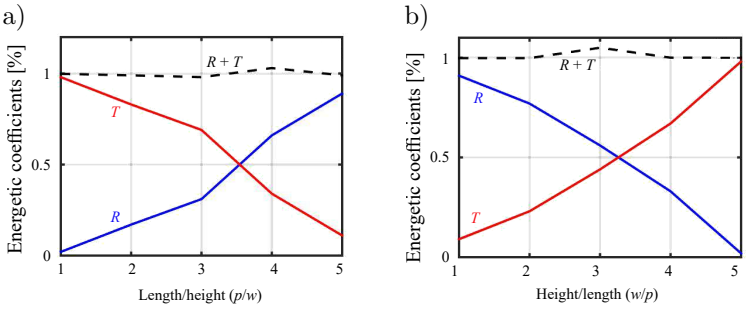

FIG. 11. Variation of the refection and transmission energy coefficients as a function of the p/w ratio (a) and the w/p ratio (b) for the cylindrical the pipe.

Several recent studies confirm the importance of guided-wave-based techniques for crack detection in plates and pipelines. The work of LIU *et al.* [41] stands as a major methodological reference for imaging circumferential cracks in pipes, notably through the use of full-wavefield data. More recently, SILITONGA *et al.* [42] provided a comprehensive review of Lamb-wave–based localization methods, detailing the conditions for selecting modes and frequencies to achieve optimal defect detection. SHAH *et al.* [43] demonstrated, through both experimental and numerical approaches, the capability of guided waves to detect

the growth of internal cracks in polyethylene pipes. Zhang *et al.* [44] subsequently showed that the use of electromagnetic acoustic transducers (EMATs) and circumferential shear horizontal (SH) modes enables the identification of defects hidden beneath coatings or supports, paving the way for truly non-contact inspections. Finally, Maruyama *et al.* [45] deepened the understanding of reflection and transmission phenomena at junctions in fluid-filled pipelines, highlighting the need for precise modeling to correctly interpret wave-defect interactions in complex geometries.

4. Conclusion

In this study, we simulated the propagation of UGWs in composite CFRTP components produced using the FDM 3D printing technique, employing an FEM. These structures were designed to include internal volumetric defects, such as rectangular notches and cracks, which are characteristic of FDM 3D printing. We detailed the selection of various spatial and temporal discretizing parameters, and the numerical models were created by generating analytical displacements with a Hanning window weighting across the waveguide thickness. Strategically positioned transducers captured the reflected and transmitted signals, ensuring that only propagating waves were recorded. We implemented a novel signal-processing technique based on the summation and subtraction of the captured signals to differentiate between the various modes detected. This approach proved effective for analyzing mode conversion phenomena. The accuracy of the results was evaluated through the energy balance, specifically by calculating the reflection and transmission energy coefficients. Our findings indicated that these energy coefficients are significantly influenced by the dimensions of the defects. We modeled three types of defects (positioned symmetrically or asymmetrically in relation to the propagation direction, as well as inclined defects) within composite plates and cylindrical pipes. The results demonstrate the potential of UGWs to inspect parts with internal defects arising from the FDM 3D printing process. We also conducted a study on defect dimensions and reported a novel method for determining the modal characteristics during mode conversion according to the symmetry criterion of the recorded displacements at the surfaces. Looking ahead, we will explore correlations between defect parameters and the mechanical properties of the structures, encompassing all types of modes, including both propagating and evanescent modes.

Fundings

This research did not receive any specific grant from funding agencies in the public, commercial, or not-for-profit sectors.

Conflict of interest

The authors declare that there are no known competing financial interests or personal relationships that could have influenced the work described in this paper.

Authors' contributions

Ismaine Zitouni conceptualized the study and wrote the original draft. Hassan Rhimini performed the analysis and contributed to data interpretation. Abdelkerim Chouaf contributed to data interpretation. All authors reviewed and approved the final manuscript.

References

1. Sefene E.M., State-of-the-art of selective laser melting process: a comprehensive review, *Journal of Manufacturing Systems*, **63**: 250–274, 2022, https://doi.org/10.1016/j.jmsy.2022.04.002.

2. Gueche Y.A., Sanchez-Ballester N.M., Cailleaux S., Bataille B., Soulairol I., Selective laser sintering (SLS), a new chapter in the production of solid oral forms (SOFs) by 3D printing, *Pharmaceutics*, **13**(8): 1212, 2021, https://doi.org/10.3390/pharmaceutics13081212.

3. Aourik O., Othmani M., Saadouki B., Abouzaid K., Chouaf A., Fracture toughness of ABS additively manufactured by FDM process, *Journal of Achievements in Materials and Manufacturing Engineering*, **109**(2), 2021, https://doi.org/10.5604/01.3001.0015.6258.

4. Ichihara N., Ueda M., Urushiyama Y., Todoroki A., Matsuzaki R., Hirano H., Progressive damage simulation for a 3D-printed curvilinear continuous carbon fiber-reinforced thermoplastic based on continuum damage mechanics, *Advanced Composite Materials*, **29**(5): 459–474, 2020, https://doi.org/10.1080/09243046.2020.1724430.

5. Blanco I., The use of composite materials in 3D printing, *Journal of Composites Science*, **4**(2): 42, 2020, https://doi.org/10.3390/jcs4020042.

6. Tang C., Tan J.L., Wong C.H., A numerical investigation on the physical mechanisms of single track defects in selective laser melting, *International Journal of Heat and Mass Transfer*, **126**: 957–968, 2018, https://doi.org/10.1016/j.ijheatmasstransfer.2018.06.073.

7. Zhang B., Li Y., Bai Q., Defect formation mechanisms in selective laser melting: a review, *Chinese Journal of Mechanical Engineering*, **30**(3): 515–527, 2017, https://doi.org/10.1007/s10033-017-0121-5.

8. Zupančič B., Prokop Y., Nikonov A., FEM analysis of dispersive elastic waves in three-layered composite plates with high contrast properties, *Finite Elements in Analysis and Design*, **193**: 103553, 2021, https://doi.org/10.1016/j.finel.2021.103553.

9. Rhimini H., El Allami M., Sidki M., Haddout A., Benhadou M. (2016), Ultrasonic guided waves in tri-layer structure. Application to study the interaction of guided waves with hidden defect at low frequency, *Technical Acoustics*, **16**(5): 1–14.

10. De Luca A., Sharif-Khodaei Z., Aliabadi M.H., Caputo F., Numerical simulation of the Lamb wave propagation in impacted CFRP laminate, *Procedia Engineering*, **167**: 109–115, 2016, https://doi.org/10.1016/j.proeng.2016.11.676.

11. Chiu W.K., Rose L.R.F., Nadarajah N., Scattering of the fundamental anti-symmetric Lamb wave by a midplane edge delamination in a fiber-composite laminate, *Procedia Engineering*, **188**: 317–324, 2017, https://doi.org/10.1016/j.proeng.2017.04.490

12. Everton S.K., Dickens P., Tuck C., Dutton B., Identification of sub-surface defects in parts produced by additive manufacturing, using laser generated ultrasound, [in:] *Additive Manufacturing and 3D Printing Research Group, University of Nottingham*, 2016.

13. Cummings I., Hillstrom E., Newton R., Flynn E., Wachtor A., In-process ultrasonic inspection of additive manufactured parts, [in:] *Topics in Modal Analysis & Testing, Volume 10*, pp. 235–247, 2016, https://doi.org/10.1007/978-3-319-30249-2_20.

14. Caminero M.A., García-Moreno I., Rodríguez G.P., Chacón J.M., Internal damage evaluation of composite structures using phased array ultrasonic technique: impact damage assessment in CFRP and 3D printed reinforced composites, *Composites Part B: Engineering*, **165**: 131–142, 2019, https://doi.org/10.1016/j.compositesb.2018.11.091.

15. Lee J.-M., Lee C.-J., Kim B.-M., Ko D.-C., Design of prepreg compression molding for manufacturing of CFRTP B-pillar reinforcement with equivalent mechanical properties to existing steel part, *International Journal of Precision Engineering and Manufacturing*, **21**(3): 545–556, 2020, https://doi.org/10.1007/s12541-019-00265-z.

16. Tian X., Liu T., Yang C., Wang Q., Li D., Interface and performance of 3D printed continuous carbon fiber reinforced PLA composites, *Composites Part A: Applied Science and Manufacturing*, **88**: 198–205, 2016, https://doi.org/10.1016/j.compositesa.2016.05.032.

17. Sugiyama K., Matsuzaki R., Ueda M., Todoroki A., Hirano Y., 3D printing of composite sandwich structures using continuous carbon fiber and fiber tension, *Composites Part A: Applied Science and Manufacturing*, **113**: 114–121, 2018, doi: https://doi.org/10.1016/j.compositesa.2018.07.029.

18. Takeda N., Ogihara S., Kobayashi A., Microscopic fatigue damage progress in CFRP cross-ply laminates, *Composites*, **26**(12): 859–867, 1995, https://doi.org/10.1016/0010-4361(95)90879-5.

19. Nairn J.A., 2.12 – Matrix microcracking in composites, *Comprehensive Composite Materials*, **2**: 403–432, 2000, https://doi.org/10.1016/B0-08-042993-9/00069-3.

20. Zitouni I., Rhimini H., Chouaf A., Comparative study of matrix methods for modeling the dispersive character of ultrasonic guided waves, *Engineering Transactions*, **73**(2): 305–321, 2025, https://doi.org/10.24423/engtrans.3493.2025.

21. Zitouni I., Rhimini H., Chouaf A., Modeling the propagation of ultrasonic guided waves in a composite plate by a spectral approximation method, *Engineering Transactions*, **71**(2): 213–227, 2023, https://doi.org/10.24423/EngTrans.3073.20230510.

22. Zitouni I., Rhimini H., Chouaf A., A combined Newton–bisection approach for calculating the dispersion curves in anisotropic multilayered waveguides, *Journal of Vibration Engineering & Technologies*, **12**: 5189–5201, 2024, https://doi.org/10.1007/s42417-023-01191-1.

23. Zitouni I., Rhimini H., Chouaf A., Spectral method for modeling the dispersion of complex guided wave modes in anisotropic pipeline, *Journal of Computational Applied Mechanics*, **55**(3): 473–484, 2024, https://doi.org/10.22059/jcamech.2024.376537.1090.

24. Benmeddour F., Grondel S., Assaad J., Moulin E., Experimental study of the A_0 and S_0 Lamb waves interaction with symmetrical notches, *Ultrasonics*, **49**(2): 202–205, 2009, https://doi.org/10.1016/j.ultras.2008.08.002.

25. Wandowski T., Malinowski P., Kudela P., Ostachowicz W., Analysis of S0/A0 guided wave mode conversion phenomenon, [in:] *SPIE 10600, Health Monitoring of Structural and Biological Systems XII*, 2018, https://doi.org/10.1117/12.2295001.

26. Liu G., Qu J., Guided circumferential waves in a circular annulus, *Journal of Applied Mechanics*, **65**(2): 424–430, 1998, https://doi.org/10.1115/1.2789071.

27. Nayfeh A.H., The general problem of elastic wave propagation in multilayered anisotropic media, *The Journal of the Acoustical Society of America*, **89**(4): 1521–1531, 1991, https://doi.org/10.1121/1.400988.

28. Hashamdar H., Ibrahim Z., Jameel M., Finite element analysis of nonlinear structures with Newmark method, *International Journal of the Physical Sciences*, **6**(6): 1395–1403, 2011.

29. El Allami M., Rhimini H., Sidki M., Application of the Complex Mother Wavelet Shan 1-1.5 processing to Lamb modes signals in plates, *International Journal of Science and Research (IJSR)*, **4**(1): 1849–1854, 2015.

30. Moser F., Jacobs L.J., Qu J., Modeling elastic wave propagation in waveguides with the finite element method, *NDT & E International*, **32**(4): 225–234, 1999, https://doi.org/10.1016/S0963-8695(98)00045-0.

31. Mohseni H., Ng C.-T., Rayleigh wave propagation and scattering characteristics at debondings in fibre-reinforced polymer-retrofitted concrete structures, *Structural Health Monitoring*, **18**(1): 303–317, 2019, https://doi.org/10.1177/1475921718754371.

32. Pant U., Banerjee S. (2022), Numerical modelling of ultrasonic guided waves for detection and characterisation of debonds in FRP strengthened beams, [in:] *International Symposium on Non-Destructive Testing in Civil Engineering (NDT-CE 2022)*, **27**(9), 2022, https://doi.org/10.58286/27290.

33. Zheng M.-F., Lu C., Chen G.-Z., Men P., Modeling three-dimensional ultrasonic guided wave propagation and scattering in circular cylindrical structures using finite element approach, *Physics Procedia*, **22**: 112–118, 2011, https://doi.org/10.1016/j.phpro.2011.11.018.

34. Nayfeh A.H., The general problem of elastic wave propagation in multilayered anisotropic media, *The Journal of the Acoustical Society of America*, **89**(4): 1521–1531, 1991, https://doi.org/10.1121/1.400988.

35. Podder P., Khan T.Z., Khan M.H., Rahman M.M., Comparative performance analysis of Hamming, Hanning and Blackman window, *International Journal of Computer Applications*, **96**(18): 1–7, 2014, https://doi.org/10.5120/16891-6927.

36. Ismaine Z., Hassan R., Abdelkerim C., New spectral displacement post-processing approach for modeling ultrasonic guided waves, [in:] *2023 3rd International Conference on Innovative Research in Applied Science, Engineering and Technology (IRASET)*, 2023, https://doi.org/10.1109/IRASET57153.2023.10152927.

37. Ismaine Z., Hassan R., Abdelkerim C. (2025), Hybrid spectral approach for ultrasonic guided wave dispersion in fluid-loaded anisotropic viscoelastic multilayered structures, *Journal of Vibration Engineering & Technologies*, **13**: 565, 2025, https://doi.org/10.1007/s42417-025-02120-0.

38. Väer K., Anton J., Klauson A., Eerme M., Őunapuu E., Tšukrejev P., Material characterization for laminated glass composite panel, *Journal of Achievements in Materials and Manufacturing Engineering*, **81**(1), 2017, https://doi.org/10.5604/01.3001.0010.2032.

39. Zhu C., Xu Y., Lu H., Pipeline unidirectional guided wave generation based on a hybrid piezoelectric transducer ring and wave-packet modification, *Journal of Pipeline Science and Engineering*, **6**(2): 100416, 2026, https://doi.org/10.1016/j.jpse.2025.100416.

40. Zitouni I., Rhimini H., Chouaf A., Integration of piezoelectric wafer sensors PWS signal to generate ultrasonic guided waves in planar and cylindrical waveguide, *Periodica Polytechnica Mechanical Engineering*, **69**(1): 83–91, 2025, https://doi.org/10.3311/PPme.39665.

41. Liu K., Wu Z., Jiang Y., Wang Y., Zhou K., Chen Y., Guided waves based diagnostic imaging of circumferential cracks in small-diameter pipe, *Ultrasonics*, **65**: 34–42, 2016, https://doi.org/10.1016/j.ultras.2015.10.025.

42. Silitonga D.J., Declercq N.F., Walaszek H., Vu Q.A., Saidoun A., Samet N., Ndiaye E.B., Thabourey J., A comprehensive study of non-destructive localization of structural features in metal plates using single and multimodal Lamb wave excitations, *Acta Acustica*, **8**: 66, 2024, https://doi.org/10.1051/aacus/2024069.

43. Shah J.K., Wang H., El-Hawwat S., Detection of internal crack growth in polyethylene pipe using guided wave ultrasonic testing, *Earthquake Engineering and Engineering Vibration*, **23**: 319–329, 2024, https://doi.org/10.1007/s11803-024-2238-8.

44. Zhang X., Zhou J., Hu Y., Liu Y., Shen X., Electromagnetic acoustic detection of pipe defects hidden above T-type support structures with circumferential shear horizontal guided wave, *Micromachines*, **15**(4): 550, 2024, https://doi.org/10.3390/mi15040550.

45. Maruyama T., Matsuo T., Nakahata K., Numerical study on guided-wave reflection and transmission at water pipe joint using hybrid finite element method, *Computational Mechanics*, **75**: 285–300, 2025, https://doi.org/10.1007/s00466-024-02505-0.

Received June 26, 2025; revised January 12, 2026; accepted January 15, 2026; available online January 26, 2026; version of record July 10, 2026; published issue XXXX.